processes

MDPI

Article

Kinetics on Chromium-Bearing Vanadia-Titania Magnetite Smelting with High-Basicity Pellet

Hanlin Song [1,2,3,4], Jinpeng Zhang [1,2,3,4] and Xiangxin Xue [1,2,3,4,*]

[1] School of Metallurgy, Northeastern University, Shenyang 110819, China; 1710496@stu.neu.edu.cn (H.S.); 1801576@stu.neu.edu.cn (J.Z.)
[2] Liaoning Key Laboratory of Recycling Science for Metallurgical Resources, Shenyang 110819, China
[3] Innovation Research Institute of Vanadium and Titanium Resource Industry Technology, Northeastern University, Shenyang 110819, China
[4] Innovation Research Institute of Comprehensive Utilization Technology for Vanadium-Titanium Magnetite Resources in Liaoxi District, Chaoyang 122000, China
* Correspondence: xuexx@mail.neu.edu.cn

Abstract: The effects of high-basicity pellet on smelting chromium-bearing vanadia-titania magnetite are investigated via thermodynamic smelting and non-isothermal kinetics experiments. The thermodynamic results indicated that the high-basicity pellet significantly affects and ameliorates the softening-melting-dripping behaviors during the smelting process. As the high-basicity pellet ratio increased from 0 wt.% to 52 wt.%, the range of softening temperature [T_{40}–T_4] decreased from 121 °C to 84 °C and the melting-dripping temperature [T_d–T_s] decreased from 224 °C to 169 °C. Moreover, the apparent activation energy of non-isothermal kinetics also decreased from 99.91 kJ·mol^{-1} to 66.74 kJ·mol^{-1}. Additionally, the reaction mechanism of high-basicity pellet on smelting chromium-bearing vanadia-titania magnetite was investigated via thermodynamic calculations of Gibbs free energy and characterizations of the titanium slag. Therefore, combined with the lowest permeability index, the fastest non-isothermal reduction rate, the highest recovery of valuable elements and the minimum content of titanium carbonitride, the preferable high-basicity pellet ratio was considered to be 11~23 wt.%.

Keywords: kinetics; non-isothermal; high-basicity pellet; chromium-bearing vanadia-titania magnetite; apparent activation energy

check for updates

Citation: Song, H.; Zhang, J.; Xue, X. Kinetics on Chromium-Bearing Vanadia-Titania Magnetite Smelting with High-Basicity Pellet. *Processes* **2021**, *9*, 811. https://doi.org/10.3390/pr9050811

Academic Editor: Chi-Min Shu

Received: 12 April 2021
Accepted: 4 May 2021
Published: 6 May 2021

Publisher's Note: MDPI stays neutral with regard to jurisdictional claims in published maps and institutional affiliations.

Copyright: © 2021 by the authors. Licensee MDPI, Basel, Switzerland. This article is an open access article distributed under the terms and conditions of the Creative Commons Attribution (CC BY) license (https://creativecommons.org/licenses/by/4.0/).

1. Introduction

As a unique polymetallic resource, chromium-bearing vanadia-titania magnetite (CVTM) contains iron, vanadia, titania and has associated chromium resources with a highly comprehensive utilization value. Moreover, the blast furnace process for the comprehensive utilization of chromium-bearing vanadia-titania magnetite based on pyrometallurgy separation has been systematically established in China [1,2]. However, the titanium dioxide is easily over-reduced to titanium carbonitride in the smelting process, which will cause slag thickening, slag foaming and slag-iron mixing [3–6]. For the CVTM blast furnace smelting behavior with a high-basicity pellet, few corresponding kinetics studies have been conducted. There have been many kinetics studies on a single reduction or oxidation of VTM powders or pellet or sinter, but in terms of the calculation methods of reduction rate, kinetics models, activation energy and judging standards for limitations are quite different [7–14]. More importantly, the pellet and sinter coexist and interact in the blast furnace smelting process. The reduction kinetics of a single sample cannot directly guide the blast furnace smelting production of CVTM. Therefore, this study attempts to reveal the metallurgical reaction kinetics of CVTM smelting with a high-basicity pellet.

2. Materials and Methods

2.1. Materials Preparation

At present, high-basicity sinter, acid pellet and lump ore are still the main burden structures for CVTM smelting in blast furnaces. The experimental samples consisted of an acid pellet and high-basicity pellet/sinter at the mass ratio of 1:1.2 to obtain the slag basicity required by actual production (R = CaO/SiO_2 = 1.1). The basic pellet replaces 0 wt.%, 25 wt.%, 50 wt.%, 75 wt.%, and 100 wt.% of the high-basicity sinter, respectively. Therefore, the ratio of basic pellet in the samples was 0 wt., 11 wt.%, 18 wt.%, 23 wt.% and 52 wt.%, respectively. These ratios were marked in the figures and tables as condition numbers of 1, 2, 3, 4 and 5, respectively. The acid CVTM pellets were prepared in an air atmosphere by pre-baking at 900 °C for 15 min and then calcining at 1200 °C for 20 min. The basic pellets were produced by pre-baking at 950 °C for 15 min and then calcining at 1250 °C for 20 min. The XRD pattern and chemical components of concentrates fines, acid pellet (AP), high-basicity sinter (BS) and high-basicity pellet (BP) are shown in Table 1.

Table 1. The chemical component of CVTM ore, pellet and sinter.

CVTM	TFe	CaO	MgO	SiO_2	Al_2O_3	TiO_2	V_2O_5	Cr_2O_3
Concentrate fines	53.350	0.960	3.330	4.710	2.820	11.600	1.143	0.810
BS (R = 1.90)	46.669	9.540	3.324	5.016	2.920	10.145	0.975	1.003
BP (R = 2.01)	48.346	9.380	3.044	4.675	2.672	10.512	1.035	0.734
AP (R = 0.19)	52.822	0.991	3.326	5.108	2.920	11.485	1.131	0.802

2.2. Apparatus and Methods

According to the national test standard GB/T 34211-2017, the experiments of softening-melting-dripping performances and thermogravimetric (TG) reduction were mainly carried out in the lab-level blast furnace, as shown in Figure 1. The 500 g samples were sandwiched between two sets of 100 g coke and placed in the graphite crucible (inner diameter 75 mm × height 180 mm). Their reaction conditions are shown in Figure 2. The temperature in the TG experiment was tested as a side-temperature of the furnace.

For T_4, the softening start temperature with burden shrinkage rate was 4%. For T_{40}, the softening end temperature with burden shrinkage rate was 40%. For T_s, the melting start temperature with the pressure in hearth sharply increased to 500 Pa. For T_d, the dripping start temperature with the weight of dripped substance reached 20 g. The softening zone [T_{40}–T_4] and the melting-dripping zone [T_d–T_s] showed the position of the lump zone and cohesive zone [15,16].

Apparent softening viscosity μ_a (Pa·s), the shrinking resistance of an overall packed burden bed, is defined in Equation (1). L refers to the layer thickness (m). M refers to load (Pa). t refers to reaction time (s) [17,18].

$$dL/dt = -ML/\mu_a, \quad (1)$$

The S value, the burden permeability index, was calculated by Equation (2). The ΔP refers to the real-time pressure difference. The P_s refers to the pressure difference in the smelting start temperature. The higher the S value, the worse the burden permeability.

$$S = \int (\Delta P - P_s)\, dT\ (T\colon T_s \rightarrow T_d), \quad (2)$$

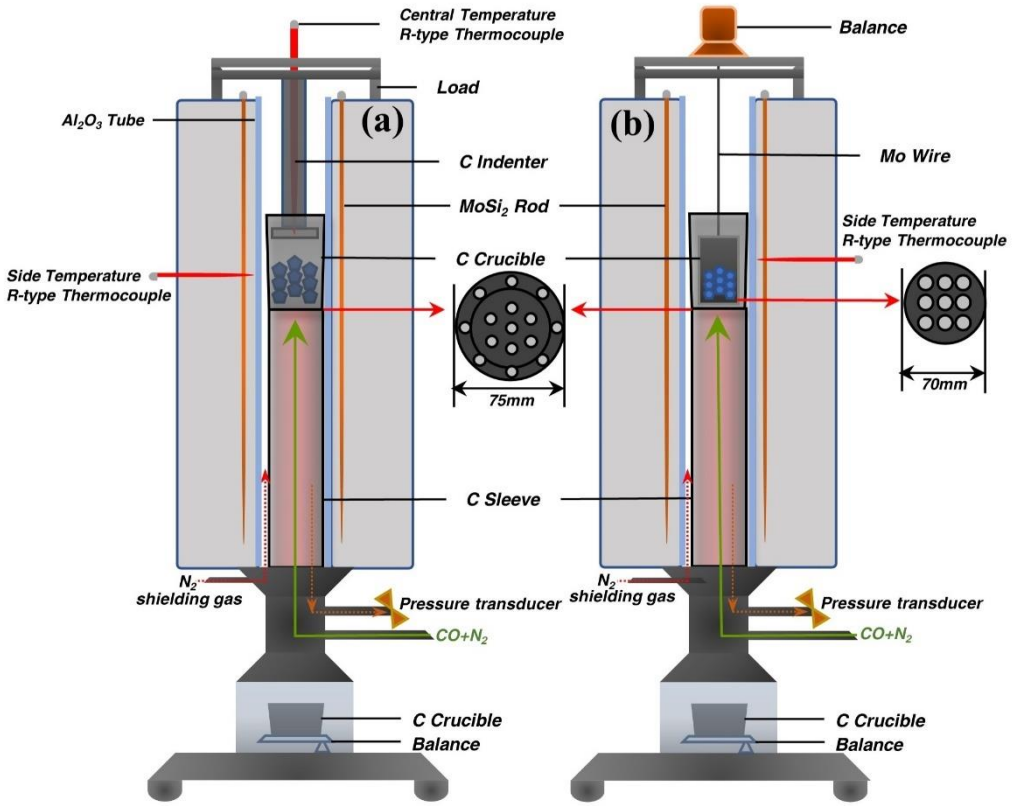


Figure 1. Apparatus: (**a**) softening-melting-dripping performances test furnace; (**b**) thermogravimetric reduction furnace.

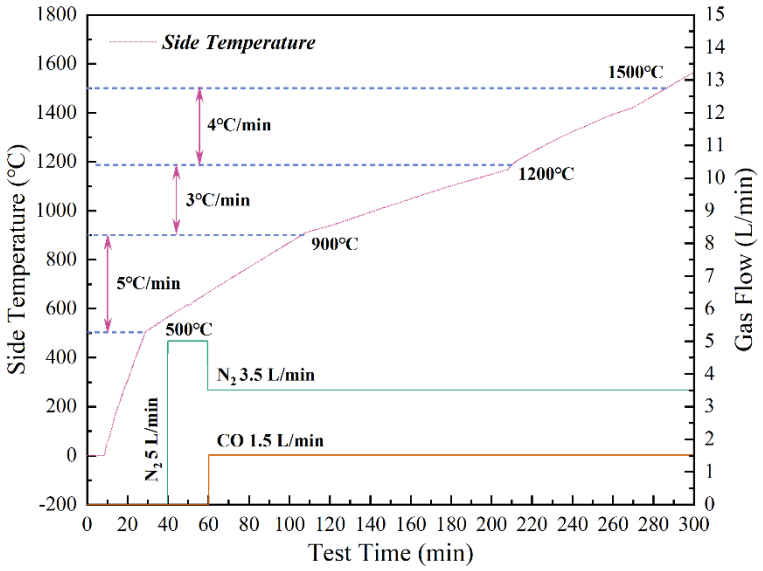


Figure 2. Reaction conditions.

2.3. Characterizations

The phases of slag and iron were analyzed by X-ray diffraction (XRD, X' Pert Pro; PANalytical, Almelo, Netherlands) with Cu Kα radiation (wavelength = 1.5406 Å) at a setting of 40 kV and 40 mA. The chemical compositions of ground samples were analyzed by inductively coupled plasma-atomic emission spectroscopy (ICP-AES, Optima 8300DV; PerkinElmer, Waltham, MA, USA) and X-ray fluorescence (XRF, ZSXPrimus II; Rigaku, Japan). The surface chemical properties of surface elements were analyzed by X-ray Photoelectron Spectroscopy (XPS, XPS peak; ESCALAB250, Thermo, Waltham, MA, USA). A scanning electron microscope (SEM, Ultra Plus; Carl Zeiss GmbH, Jena, Germany) was

used to detect the microstructure of unground slag with a backscattering detector (BSE) and energy disperse spectroscopy (EDS).

3. Results and Discussion

3.1. Effect of High-Basicity Pellet in the Thermodynamic Smelting Process

The preparation process of the pellet can greatly reduce energy consumption, environmental pollution and carbon dioxide emissions compared with sintering. It is gradually recognized to partially or even completely replace the high-basicity sinter with a high-basicity pellet. At present, there are still very few studies on using a large proportion of pellet, especially the high-basicity pellet, to replace the high-basicity sinter in CVTM smelting. Therefore, to more clearly investigate the effect of high-basicity pellets on the multi-metal system, a stable and eligible BP ratio should first be clarified. Figure 3 shows the effect of the BP ratio on the softening-melting-dripping characteristics. As the BP ratio increased from 0 wt.% to 52 wt.%, the T_4, T_{40}, T_s and T_d showed a W-shaped trend. Generally, the reduction in [T_{40}–T_4] and [T_d–T_s] means better air permeability and poor reactivity. The increase in T_4 and T_{40} means that the reactivity of the lump zone becomes worse, while the increase in T_s and T_d indicates that the higher melting point and viscosity of the slag. Therefore, the eligible BP ratio needs to consider the changes in the softening-melting-dripping characteristic parameters comprehensively. When the BP ratio increased from 0 wt.% to 18 wt.%, the T_4, T_{40}, T_s and T_d decreased by 57 °C, 69 °C, 61 °C and 89 °C, respectively and [T_{40}–T_4] and [T_d–T_s] decreased by 12 °C and 28 °C, which meant that the increase in BP ratio could significantly improve the softening-melting-dripping performances. More importantly, compared with the BP ratio of 11 wt.% and 23 wt.%, a higher [T_{40}–T_4] in the BP ratio of 18 wt.% can ensure better medium-temperature reducibility of the charge in the lamp zone. In contrast, the higher T_s and T_d and appropriate [T_d–T_s] could ensure high-temperature reactions in the cohesive zone [3–5,7,15,19–26].

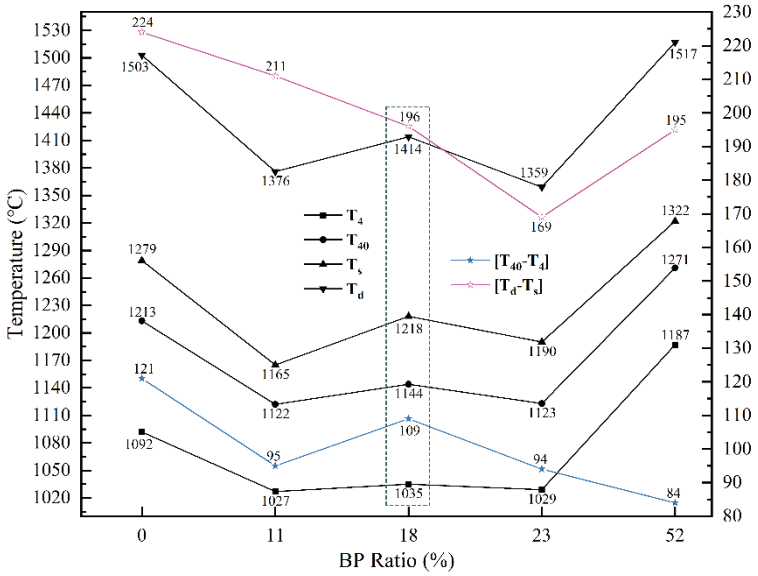


Figure 3. Softening-melting-dripping performances with different BP ratios.

The changes in the apparent softening viscosity and shrinkage rate of the burden layer can reflect the speed of reducing the lump zone. As shown in Figure 4, as the BP ratio increased from 11 wt.% to 23 wt.%, the apparent softening viscosity reached the peak value earlier than that in the BP ratio of 0 wt.% and 52 wt.%, which meant that the gas-solid reactivity of the charge layer was improved. Moreover, the coexistence of BP and BS can promote the fusion of the interphase and accelerate the softening behavior. While the BP ratios were 0 wt.% (100 wt.% BS) and 52 wt.% (100 wt.% BP), the apparent softening viscosity reached the peak later, which meant that a synergic ratio should be confirmed due to the poor mid-temperature reducibility of the 100 wt.% BP or 100 wt.% BS in the lump

zone. The S value showed the gas permeability of the melting-dripping zone (Figure 5). It could be found that the S value was the smallest when the BP ratio was 18 wt.%, which meant that the gas permeability of the burden layer was the best in this case. Moreover, as shown in Figure 6, when the BP ratio increased to 11 wt.%, the highest recovery of Cr and V increased to 0.706 wt.% and 0.25 wt.%, respectively.

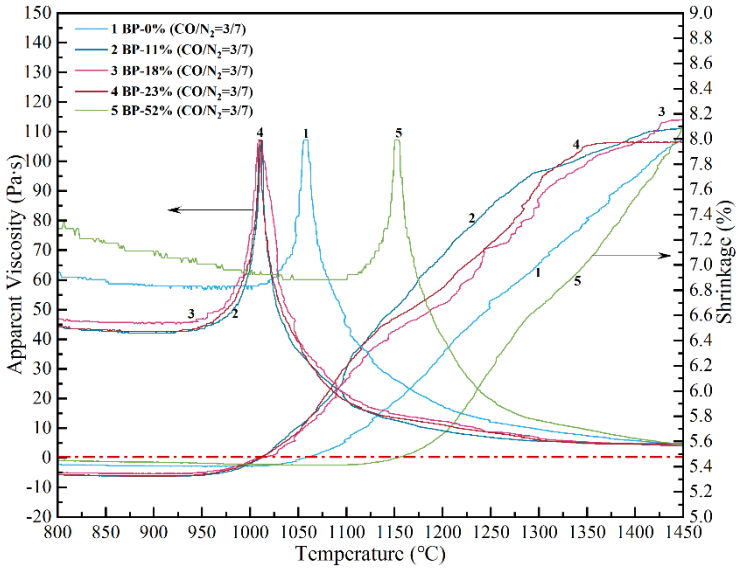


Figure 4. Apparent softening viscosity with different BP ratios.

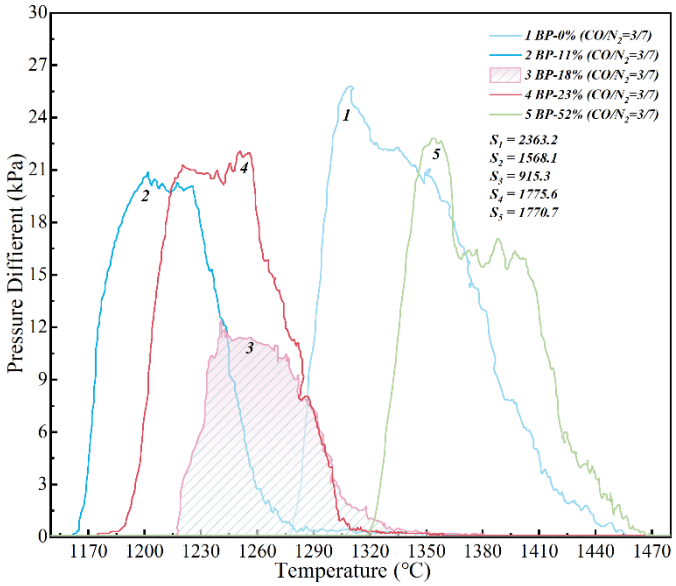


Figure 5. Gas permeability index S with different BP ratios.

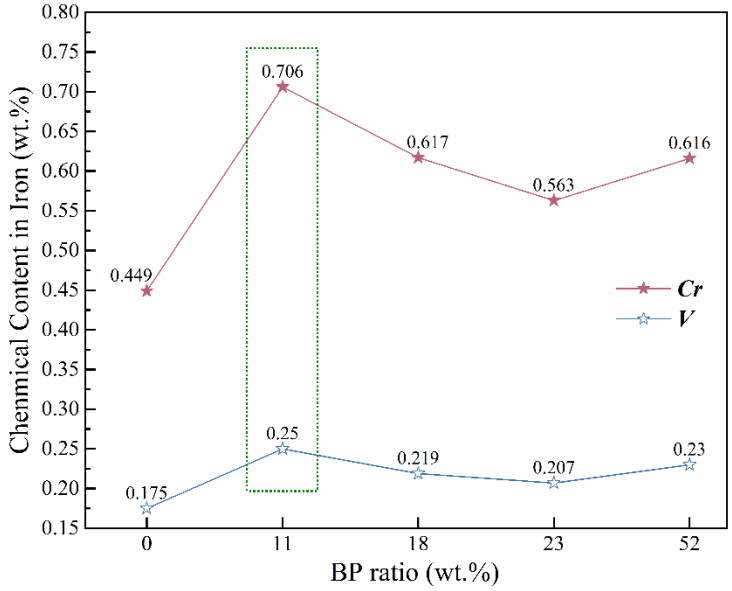


Figure 6. The content of Cr and V in the reduced iron.

3.2. Non-Isothermal Kinetics of High-Basicity Pellet in the Smelting Process

Non-isothermal kinetics experiments can reflect the complexity and activity of the interfacial reaction at different stages in the softening-melting-dripping processes and further determine the preferable BP ratio for CVTM smelting. As shown in Figure 7, the non-isothermal thermogravimetry results showed a synchronized process with the softening-melting-dripping experiments. When the temperature increased from 700 K to 1400 K, the kinetics curves showed a nonlinear variation, which meant that the complex multi-interface reactions occurred simultaneously during the CVTM smelting process.

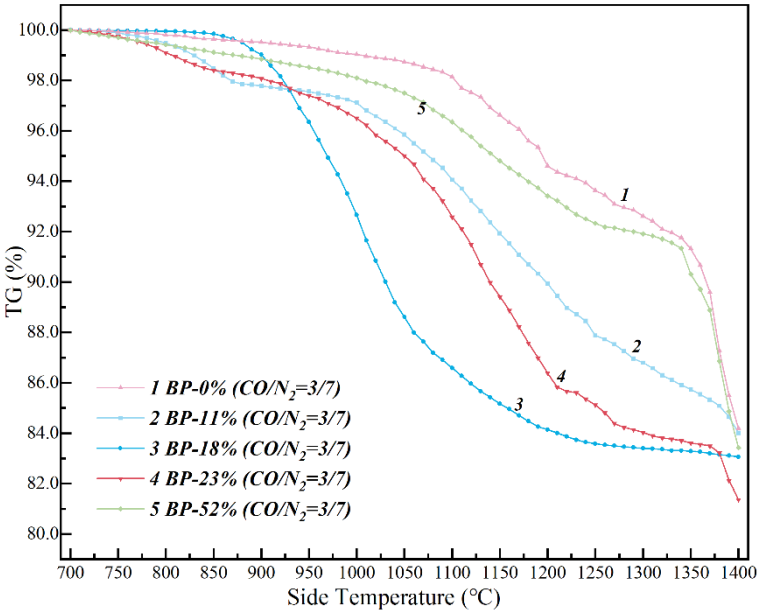


Figure 7. Multi-interface non-isothermal kinetics mass change curve.

To further analyze the non-isothermal kinetics curves, the weight loss rate α can be set to indicate the reduction rate of the charge, and the definition is shown in Equation (3).

$$\alpha = \Delta m/m_0, \quad (3)$$

The Δm is the weight loss of the sample, and the m_0 is the original weight of the sample. According to the Avrami-Erofeev model (Equation (4)), it is judged that the reduction process of the sample conforms to the n-order reaction.

$$\ln[-\ln(1-\alpha)] = n \ln t + n \ln k, \quad (4)$$

The k is the reaction rate constant, the t is the time (min) and the n is the Avrami exponent. Figure 8 shows the fitting of the ln[−ln(1 − α)]-ln t for non-isothermal. Table 2 shows the ln[−ln(1 − α)]-ln t fitting parameters of non-isothermal kinetics. The slope of the fitted line represented Avrami exponent n. The fitting slope of ln[−ln(1 − α)]-ln t for non-isothermal kinetics was between 1.3 and 2.6. Therefore, according to the common kinetics models and the value of n listed in Table 3, the non-isothermal reduction kinetics process of CVTM could be described by CG_2, A_2 and A_3 models, which meant the reduction kinetics model was more suitable for the phase interface reaction model than the random 3D/2D unreacted core model with the increase in the BP ratio [7,9–14,27].

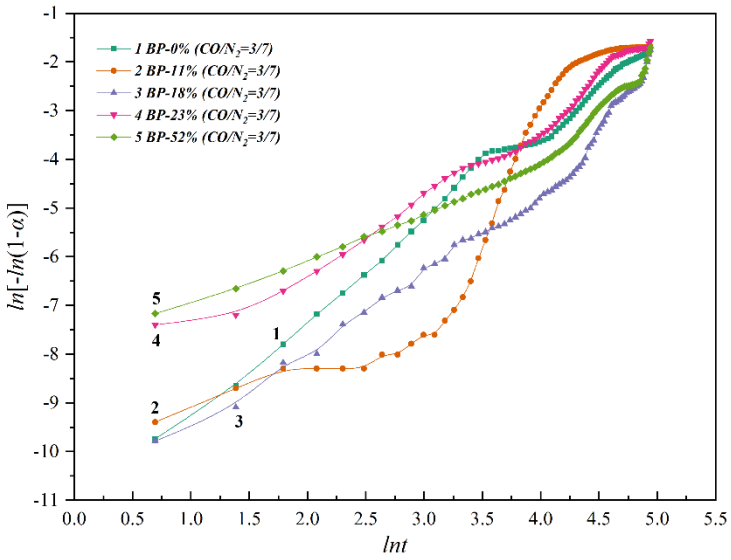


Figure 8. ln[−ln(1 − α)]-lnt fitting curve of multi-interface non-isothermal kinetics.

Table 2. Line fitting values of non-isothermal data.

Conditions	1	2	3	4	5
Slope	1.9298	1.8773	2.5804	1.5929	1.3347
Intercept	−12.087	−10.953	−13.871	−9.5373	−9.0386
R^2	0.9603	0.9906	0.893	0.9751	0.9397

Table 3. Common kinetics models.

Type	$G(\alpha)$	n
D_1	$\alpha^2 = kt$	0.62
D_2	$(1-\alpha)\ln(1-\alpha)+\alpha = kt$	0.57
D_3	$[1-(1-\alpha)^{1/3}]^2 = kt$	0.54
D_4	$(1-2/3\alpha)-(1-\alpha)^{2/3} = kt$	0.57
CG_2	$1-(1-\alpha)^{1/2} = kt$	1.11
CG_3	$1-(1-\alpha)^{1/3} = kt$	1.07
R_1	$-\ln(1-\alpha) = kt$	1.00
A_2	$[-\ln(1-\alpha)]^{1/2} = kt$	2.00
A_3	$[-\ln(1-\alpha)]^{1/3} = kt$	3.00

The Coats-Redfern equation generally solved the activation energy of the non-isothermal kinetics. When n ≠ 1, the *C-R* equation is as follows:

$$\ln\{[1-(1-\alpha)^{1-n}]/[(1-n)T^2]\} = \ln\{(AR/\beta E_a)\,[1-(2RT/E_a)]\} - E_a/RT, \quad (5)$$

The β is the heating rate (K/min), the R is the ideal gas constant with 8.314 J·mol^{-1}·K^{-1} and the T is the reaction temperature (K). The $\ln\{[1-(1-\alpha)1-n]/[(1-n)T^2]\}$ was plotted against $1/T$, as shown in Figure 9. According to the slope of the fitted line, the apparent activation energy E_a was calculated as shown in Table 4. It could be found that as the BP ratio increased, the apparent activation energy decreased from 99.91 kJ·mol^{-1} to 64.74 kJ·mol^{-1}, which meant that the reaction rate of the charge layer was accelerated in the whole process. The existence of BP was beneficial to the reduction smelting of CVTM.

Table 4. Line fitting data of non-isothermal E_a.

Conditions	1	2	3	4	5
Slope	−12017	−10800	−10217	−9445	−7786
Intercept	−9.47	−9.47	−9.46	−10.23	−12.05
R^2	0.94	0.81	0.84	0.91	0.96
E_a	99.91	89.79	84.94	78.53	64.74

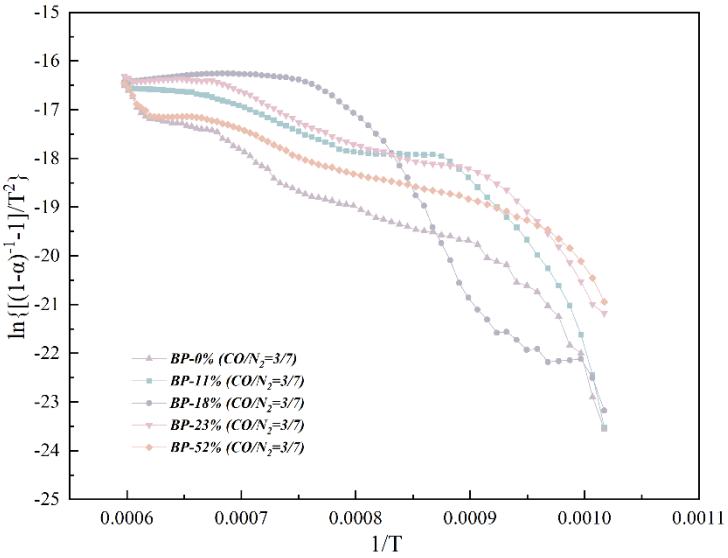


Figure 9. Coats-Redfern fitting curve of multi-interface non-isothermal kinetics.

3.3. Reaction Mechanism of High-Basicity Pellet in the Smelting Process

As shown in Equations (6) and (7), the acid pellet is mainly composed of Fe_2O_3, Fe_3O_4 and Fe_2TiO_5 during the oxidizing roasting. The high-basicity pellet is mainly composed of $CaO{\cdot}Fe_2O_3$, Fe_2O_3, $CaO{\cdot}SiO_2$, $CaO{\cdot}TiO_2$ and Fe_2TiO_5. The high-basicity sinter is mainly composed of perovskite ($CaO{\cdot}TiO_2$), 30~40% haplotypite ($mFe_2O_3{\cdot}nFeO{\cdot}TiO_2$) and 30~40% titancmagnefite ($mFe_3O_4{\cdot}n(2FeO{\cdot}TiO_2)$). The Gibbs free energy of the reduction reactions of titaniferous oxides according to the chemical equations from Equations (8)–(16) is shown in Figure 10. It can be seen that ferrotitanium oxides are complex compounds with a multi-metal structure in CVTM. Its reduction process greatly affects the softening-melting-dripping performances and kinetics process of the CVTM smelting. The reduction order of ferrotitanium oxides is: Fe_2TiO_5 ($Fe_2O_3{\cdot}TiO_2$), Fe_2TiO_4 ($2FeO{\cdot}TiO_2$), $FeTiO_3$ ($FeO{\cdot}TiO_2$) and $FeTi_2O_5$ ($FeO{\cdot}2TiO_2$). In the lump zone with a temperature ranging from 700 °C to 1200 °C, titaniferous oxides in the high-basicity pellet are mainly involved in the reactions with CaO to form $CaO{\cdot}TiO_2$ and $nCaO{\cdot}Fe_2O_3$. The thermodynamic trend sequence of new minerals formed by the reaction of calcium oxide with Fe_2O_3, TiO_2 and SiO_2 is $2CaO{\cdot}SiO_2$,

$CaO{\cdot}SiO_2$, $CaO{\cdot}TiO_2$, $2CaO{\cdot}Fe_2O_3$ and $CaO{\cdot}Fe_2O_3$. Since the sintering process includes direct reduction and re-oxidation, Fe_2TiO_5 first undergoes reduction and decomposition to produce more TiO_2. Therefore, the contact area of CaO and TiO_2 is larger, which produces more $CaO{\cdot}TiO_2$. However, perovskite increases the brittleness of the sinter, which is not conducive to improving the compressive strength of the sinter. Compared with the preparation process of the pellet, the high-basicity pellet contains less perovskite and more calcium ferrite, because most of the Fe_3O_4 is first oxidized to Fe_2O_3 and reacts preferentially with CaO to form calcium ferrite. Calcium ferrite has a low melting point, which acts as a binder phase and helps to improve the properties of pellets and sintered ore. Therefore, controlling and limiting the formation of perovskite, while promoting the formation of calcium ferrite, is of great significance for improving the strength and performance of fluxed charge. However, it should be emphasized that the preparation of sintered ore has undergone a pre-reduction process, so the low-temperature reducibility is always better that of than pellets. Therefore, it is still tough to replace the high-basicity sinter with a high-basicity pellet for blast-furnace smelting [1,2,22–25,28,29]. Due to the lower temperature and the slower solid-solid interface reactions, gas-solid reactions and gas-phase diffusion dominated the reaction process. The actual reduction process of ferrotitanium oxides is carried out simultaneously. A large amount of reduced TiO_2 not only generates perovskite but continues to be reduced to low-valence titanium oxide, titanium carbide, titanium nitride and titanium carbonitride. The performance of titanium carbonitride generated in the high-temperature zone on molten slag and molten iron would cause a sharp increase in viscosity, foaming and difficulty in separating slag and iron, which would be manifested as a worsening smelting index and higher apparent activation energy.

$$2Fe_2TiO_4 + O_2 = 2Fe_2TiO_5, \quad (6)$$

$$4FeTiO_3 + O_2 = 2Fe_2TiO_5 + TiO_2, \quad (7)$$

$$Fe_2TiO_5 + CO = Fe_2TiO_4 + CO_2,\ \Delta G_1^{\Theta} = 28309.3 - 27.11T, \quad (8)$$

$$Fe_2TiO_5 + C = Fe_2TiO_4 + CO,\ \Delta G_2^{\Theta} = 197319.3 - 199.11T, \quad (9)$$

$$Fe_2TiO_4 + CO = Fe + CO_2 + FeTiO_3,\ \Delta G_3^{\Theta} = -16550 + 26.91T, \quad (10)$$

$$Fe_2TiO_4 + C = Fe + CO + FeTiO_3,\ \Delta G_4^{\Theta} = 152460 - 145.09T, \quad (11)$$

$$2FeTiO_3 + CO = FeTi_2O_5 + Fe + CO_2,\ \Delta G_5^{\Theta} = 60277.03 + 17.07T, \quad (12)$$

$$2FeTiO_3 + C = FeTi_2O_5 + Fe + CO,\ \Delta G_6^{\Theta} = 229287.03 - 154.53T, \quad (13)$$

$$3TiO_2 + 7C + N_2 = 2TiN + TiC + 6CO,\ \Delta G_7^{\Theta} = 1{,}263{,}266 - 852.7T, \quad (14)$$

$$TiO_2 + CaO = CaO{\cdot}TiO_2,\ \Delta G_8^{\Theta} = -79900 - 3.35T, \quad (15)$$

$$Fe_2O_3 + CaO = CaO{\cdot}Fe_2O_3,\ \Delta G_9^{\Theta} = -33211 - 0.6T, \quad (16)$$

Figure 11 shows the SEM-EDS pattern of the titanium slag after the CVTM smelting. It can be found that the Ca-Si slag system is the most critical fluxed component to help promote the transfer of oxygen ions from other valuable metal compounds. A part of Fe is enriched in Mg, and Al forms a spinel phase. Most of the Ti and a part of the iron form a ferrotitanium solid solution, and the V and Cr are also relatively enriched in it. Therefore, the reduction in ferrotitanium oxides significantly affects the thermodynamic smelting characteristics and kinetic process of CVTM. Figure 12 shows the XRD pattern of titanium slag after CVTM smelting. It can be found that as the proportion of BP increases, the content of titanium carbonitrides and low-valence titanium oxide gradually decreases, while the content of FeOx increases. When the content of FeOx increases, the oxygen potential in the slag increases, which inhibits the over-reduction process of titanium oxide and the generation of titanium carbonitride. To verify and analyze the content change of titanium carbonitride, Figure 13 shows the valence state of the titanium compound in the CVTM smelting process. The ratio of $Ti2p_{3/2}$-TiN decreased as the ratio of BP increased.

Specifically, the ratio of $Ti2p_{3/2}$-TiN decreased from 11.72% to 4.89%. Figure 14 shows the content of TiO_2 and TiN in the titanium slag. With the increase in BP content, the TiO_2 content in the titanium slag increased from 25.45 wt.% to 29.18 wt.%. According to the Ti2p3/2-TiN ratio, it was calculated that the TiN content in the titanium slag decreased from 2.98 wt.% to 1.37 wt.%. In the actual CVTM smelting process, when the proportion of titanium carbonitrides approaches 3%, the viscosity of the titanium slag begins to increase sharply. Therefore, when the BP ratio is 23 wt.%, the smelting process of CVTM can be effectively improved.

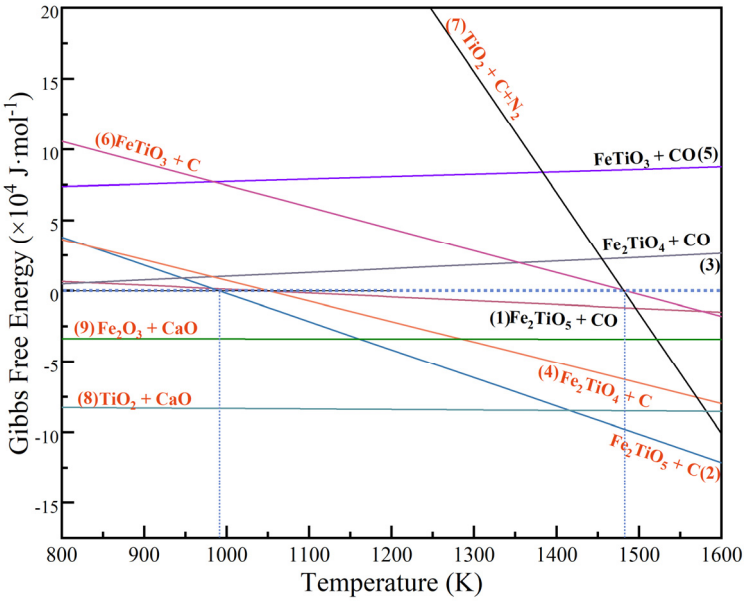


Figure 10. Gibbs free energy of the reduction reactions of titaniferous oxides.

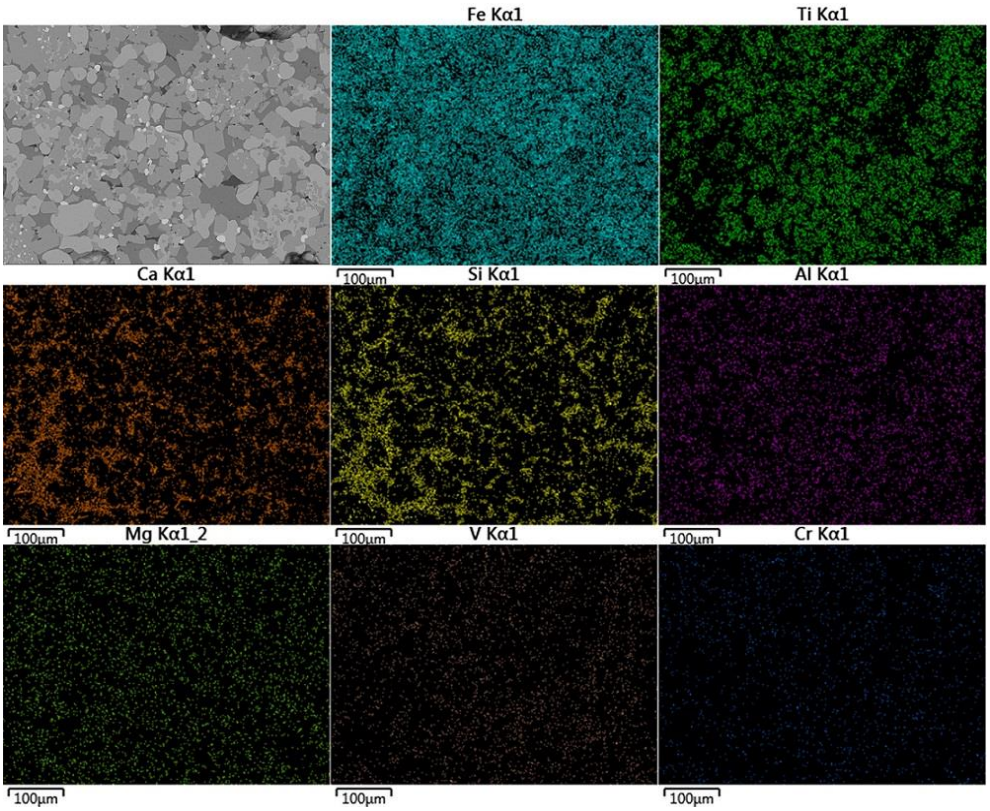


Figure 11. SEM-EDS pattern of the titanium slag after CVTM smelting.

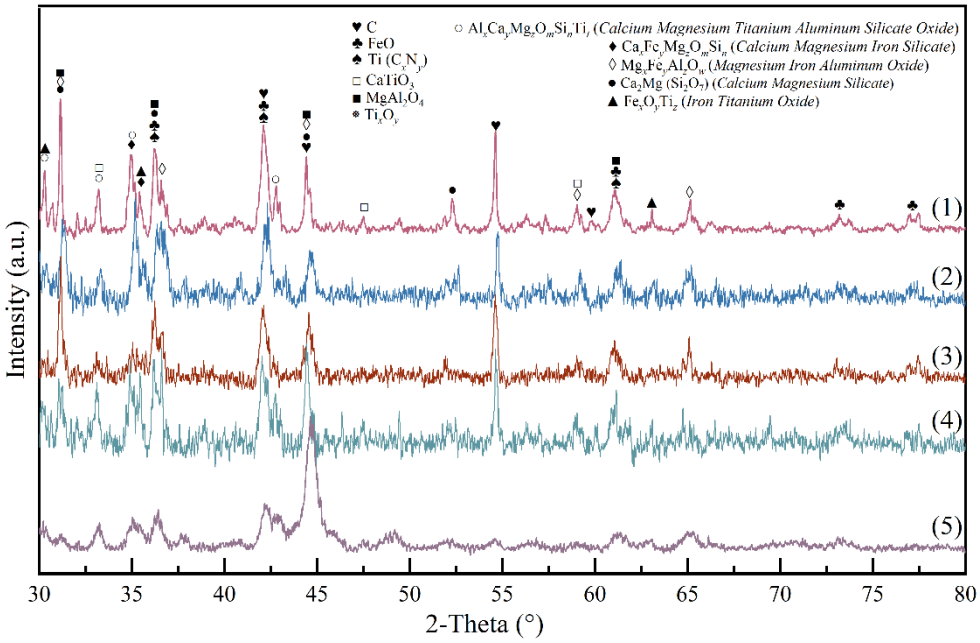


Figure 12. XRD pattern of titanium slag after CVTM smelting.

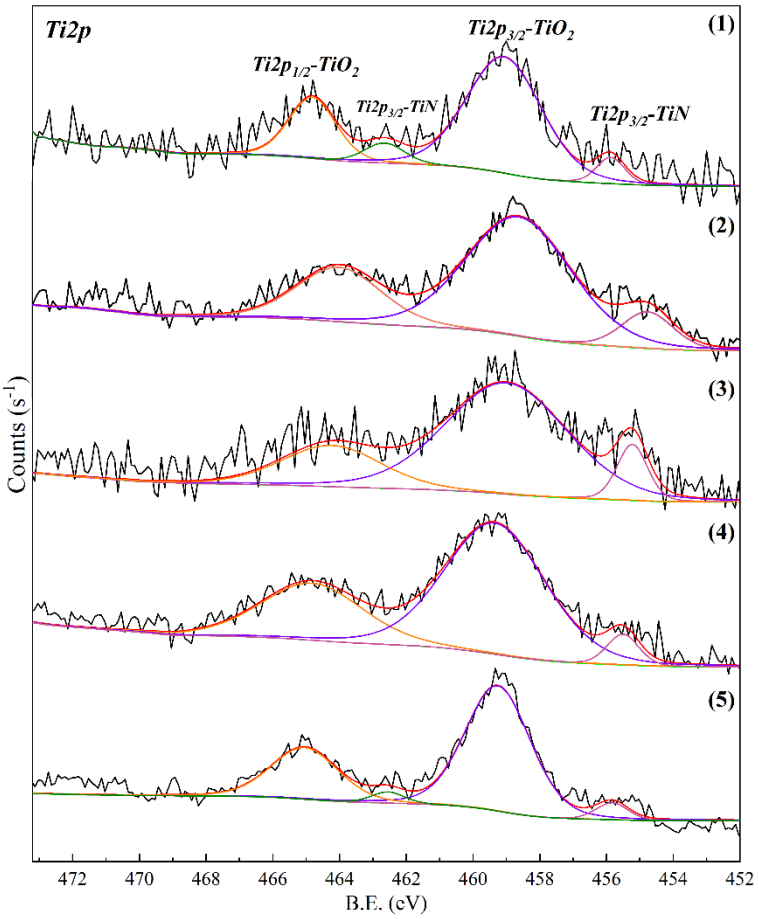


Figure 13. XPS pattern of the titanium slag after CVTM smelting.

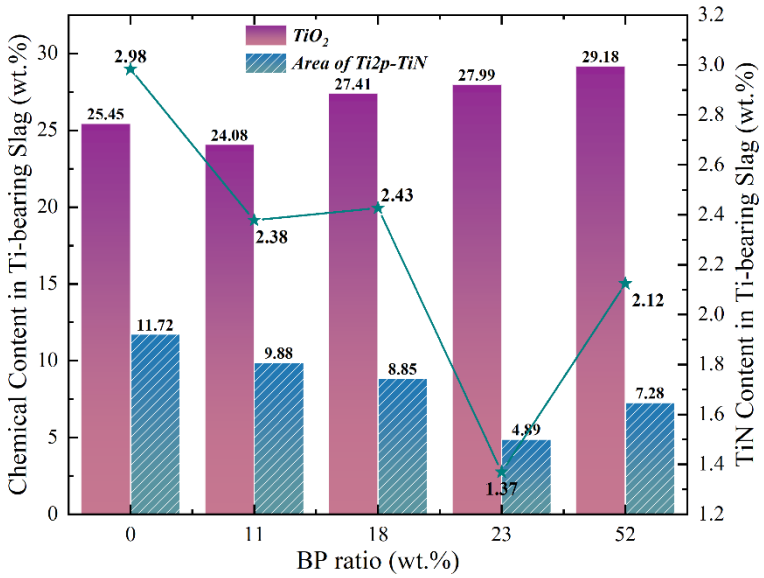


Figure 14. The content of TiO_2 and TiN in the titanium slag.

In summary, a preferable BP ratio is determined based on thermodynamic melting experiments, non-isothermal kinetic experiments and thermodynamic calculations and characterization. Using high basicity pellets (11~23 wt.%) to replace part of the sinter is beneficial for CVTM smelting. However, a specific appropriate BP ratio also depends on the thermodynamic parameters, the permeability index, the recovery of valuable elements and the content of titanium carbonitride.

4. Conclusions

(1) The preferable high-basicity pellet ratio is considered to be 18 wt.% according to the thermodynamic smelting experiments of chromium-bearing vanadia-titania magnetite. The experimental results of softening-melting-dripping characteristics showed as the ratio of high-basicity pellet increased from 0 wt.% to 52 wt.%, the softening zone [T_{40}–T_4] decreased from 121 °C to 84 °C and the melting-dripping zone [T_d–T_s] decreased from 224 °C to 169 °C. Based on the above results and combined with the lowest permeability index, a preferable high-basicity pellet ratio should be a ratio of 18 wt.%.

(2) The non-isothermal reduction kinetics process of CVTM could be described by CG_2, A_2 and A_3 models. It could be found that as the BP ratio increased, the apparent activation energy decreased from 99.91 kJ·mol^{-1} to 64.74 kJ·mol^{-1}, which meant that the reaction rate of the charge layer was accelerated in the whole process. The existence of BP was beneficial to the reduction smelting of CVTM.

(3) The reaction mechanism of high-basicity pellet on polymetallic smelting process according to thermodynamics and characterizations was investigated. Most of the Ti and a part of the iron formed a ferrotitanium solid solution, and the reduction in ferrotitanium oxides significantly affected the thermodynamic smelting characteristics and kinetic process of CVTM. When the BP ratio was 23 wt.%, the content of TiN in the titanium slag decreased from 2.98 wt.% to 1.37 wt.%.

Therefore, using high basicity pellets (11~23 wt.%) to replace part of the sinter is beneficial for CVTM smelting. However, a specific appropriate BP ratio also depends on the thermodynamic parameters, the permeability index, the recovery of valuable elements and the content of titanium carbonitride.

Author Contributions: Data curation, Software, Formal analysis, Visualization, Writing—original draft preparation and Writing—review and editing, H.S.; Data curation, Writing—Review and editing and Supervision, J.Z.; Conceptualization, Funding acquisition, Investigation, Project administration,

Resources and Supervision, X.X. All authors have read and agreed to the published version of the manuscript.

Funding: The research was financially supported by the National Natural Science Foundation of China (grant no. 51674084, no. ZX20200031 and no. 2017YFB0304304).

Institutional Review Board Statement: Not applicable.

Informed Consent Statement: Not applicable.

Data Availability Statement: Not applicable.

Acknowledgments: Special thanks are due to the Analytical and Testing Center, Northeastern University, for the instrumental analysis.

Conflicts of Interest: The authors declare no conflict of interest.

References

1. Du, H.G. *Principle of Smelting Vanadium-Titanium Magnetite*, 1st ed.; Science Press: Beijing, China, 1996.
2. Xue, X.Y.; Yang, S.T.; Zhang, Y. *Blast Furnace Process Smelting Chromium-Containing Vanadia-Titania Magnetite: Theory and Practice*, 1st ed.; Science Press: Beijing, China, 2020.
3. Cheng, G.J.; Xue, X.X.; Jiang, T.; Duan, P.N. Effect of TiO_2 on the Crushing Strength and Smelting Mechanism of High-Chromium Vanadium-Titanium Magnetite Pellets. *Metall. Mater. Trans. B* **2016**, *47*, 1713–1726. [CrossRef]
4. Li, T.L.; Sun, C.Y.; Lan, D.; Song, J.; Song, S.; Wang, Q. Effect of Mineral Elements Migration on Softening-melting Properties of Ti-bearing High Basicity Sinter. *ISIJ Int.* **2019**, *59*, 245–252. [CrossRef]
5. Liu, J.X.; Cheng, G.J.; Liu, Z.G.; Chu, M.S.; Xue, X.X. Softening and melting properties of different burden structures containing high chromic vanadium titano-magnetite. *Int. J. Miner. Process.* **2015**, *142*, 113–118. [CrossRef]
6. Yue, H.R.; He, Z.W.; Jiang, T.; Duan, P.N.; Xue, X.X. Rheological Evolution of Ti-Bearing Slag with Different Volume Fractions of TiN. *Metall. Mater. Trans. B* **2018**, *49*, 2118–2127. [CrossRef]
7. Halli, P.; Taskinen, P.; Eric, R.H. Mechanisms and Kinetics of Solid State Reduction of Titano Magnetite Ore with Methane. *J. Sustain. Metall.* **2017**, *3*, 191–206. [CrossRef]
8. Liu, S.S.; Guo, Y.F.; Qiu, G.Z.; Jiang, T.; Chen, F. Solid-state reduction kinetics and mechanism of pre-oxidized vanadium-titanium magnetite concentrate. *Trans. Nonferrous Met.. Soc.* **2014**, *24*, 3372–3377. [CrossRef]
9. Lu, C.Y.; Zou, X.L.; Lu, X.G.; Xie, X.L.; Zheng, K.; Xiao, W.; Cheng, H.W.; Li, G.S. Reductive kinetics of Panzhihua ilmenite with hydrogen. *Trans. Nonferrous Met.. Soc.* **2016**, *26*, 3266–3273. [CrossRef]
10. Lv, W.; Lv, X.W.; Zhang, Y.Y.; Li, S.P.; Tang, K.; Song, B. Isothermal oxidation kinetics of ilmenite concentrate powder from Panzhihua in air. *Powder Technol.* **2017**, *320*, 239–248. [CrossRef]
11. Pan, F.; Zhu, Q.S.; Du, Z.; Sun, H.Y. Oxidation Kinetics, Structural Changes and Element Migration during Oxidation Process of Vanadium-titanium Magnetite Ore. *J. Iron Steel Res. Int.* **2016**, *23*, 1160–1167. [CrossRef]
12. Sarkar, B.K.; Samanta, S.; Dey, R.; Das, G.C. A study on reduction kinetics of titaniferous magnetite ore using lean grade coal. *Int. J. Miner. Process.* **2016**, *152*, 36–45. [CrossRef]
13. Sui, Y.L.; Guo, Y.F.; Jiang, T.; Qiu, G.Z. Reduction kinetics of oxidized vanadium titano-magnetite pellets using carbon monoxide and hydrogen. *J. Alloys Compd.* **2017**, *706*, 546–553. [CrossRef]
14. Zhang, J.L.; Xing, X.D.; Cao, M.M.; Jiao, K.X.; Wang, C.L.; Ren, S. Reduction Kinetics of Vanadium Titano-Magnetite Carbon Composite Pellets Adding Catalysts Under High Temperature. *J. Iron Steel Res. Int.* **2013**, *20*, 1–7. [CrossRef]
15. Liu, Z.G.; Chu, M.S.; Wang, H.T.; Zhao, W.; Xue, X.X. Effect of MgO content in sinter on the softening-melting behavior of mixed burden made from chromium-bearing vanadium-titanium magnetite. *Int. J. Min. Met. Mater.* **2016**, *23*, 25–32. [CrossRef]
16. Zhao, W.; Chu, M.S.; Wang, H.T.; Liu, Z.G.; Tang, Y.T. Novel blast furnace operation process involving charging with low-titanium vanadium-titanium magnetite carbon composite hot briquette. *Int. J. Min. Met. Mater.* **2016**, *23*, 501–510. [CrossRef]
17. Song, H.L.; Zhang, J.P.; Cheng, G.J.; Yang, S.T.; Xue, X.X. The Effect of Abandoned Basic Oxygen Furnace Gas Blowing on the Softening-Melting-Dripping Performance of Full High Cr-Bearing Vanadia-Titania Magnetite Pellets. *Steel Res. Int.* **2020**, *91*, 1900501. [CrossRef]
18. Song, H.L.; Zhang, J.P.; Cheng, G.J.; Yang, S.T.; Xue, X.X. CO_2 injection improves the high-temperature performances of Cr-bearing vanadia-titania magnetite smelting in blast furnace. *J. CO2 Util.* **2021**, *43*, 101363. [CrossRef]
19. An, X.W.; Wang, J.S.; Lan, R.Z.; Han, Y.H.; Xue, Q.G. Softening and Melting Behavior of Mixed Burden for Oxygen Blast Furnace. *J. Iron Steel Res. Int.* **2013**, *20*, 11–16. [CrossRef]
20. Nandy, B.; Chandra, S.; Bhattacharjee, D.; Ghosh, D. Assessment of blast furnace behaviour through softening-melting test. *Ironmak. Steelmak.* **2006**, *33*, 111–119. [CrossRef]
21. Qie, Y.N.; Lyu, Q.; Liu, X.J.; Li, J.P.; Lan, C.C.; Zhang, S.H.; Yan, C.J. Effect of Hydrogen Addition on Softening and Melting Reduction Behaviors of Ferrous Burden in Gas-Injection Blast Furnace. *Metall. Mater. Trans. B* **2018**, *49*, 2622–2632. [CrossRef]
22. Yang, D.; Zhang, F.; Wang, J.; Yan, Z.M.; Pei, G.S.; Qiu, G.B.; Lv, X.W. Effect of Cr_2O_3 content on viscosity and phase structure of chromium-containing high-titanium blast furnace slag. *J. Mater. Res. Technol.* **2020**, *9*, 12673–12681. [CrossRef]

23. Liu, X.L.; Honeyands, T.; Evans, G.; Zulli, P.; O'Dea, D. A review of high-temperature experimental techniques used to investigate the cohesive zone of the ironmaking blast furnace. *Ironmak. Steelmak.* **2019**, *46*, 953–967. [CrossRef]
24. Xiang, J.Y.; Wang, J.; Li, Q.J.; Shan, C.; Qiu, G.B.; Yu, W.Z.; Lv, X.W. Slag-foaming phenomenon originating from reaction of titanium-bearing blast furnace slag: Effects of TiO_2 content and basicity. *Can. Metall. Quart.* **2020**, *59*, 151–158. [CrossRef]
25. Hu, K.; Tang, K.; Lv, X.W.; Safarian, J.; Yan, Z.M.; Song, B. Modeling Viscosity of High Titania Slag. *Metall. Mater. Trans. B* **2021**, *52*, 245–254. [CrossRef]
26. Li, W.; Wang, N.; Fu, G.Q.; Chu, M.S.; Zhu, M.Y. Influence of TiO_2 addition on the oxidation induration and reduction behavior of Hongge vanadium titanomagnetite pellets with simulated shaft furnace gases. *Powder Technol.* **2018**, *326*, 137–145. [CrossRef]
27. Zhao, L.S.; Wang, L.N.; Chen, D.S.; Zhao, H.X.; Liu, Y.H.; Qi, T. Behaviors of vanadium and chromium in coal-based direct reduction of high-chromium vanadium-bearing titanomagnetite concentrates followed by magnetic separation. *Trans. Nonferrous Met. Soc.* **2015**, *25*, 1325–1333. [CrossRef]
28. Malinauskaite, J.; Jouhara, H.; Czajczynska, D.; Stanchev, P.; Katsou, E.; Rostkowski, P.; Thorne, R.J.; Colon, J.; Ponsa, S.; Al-Mansour, F.; et al. Municipal solid waste management and waste-to-energy in the context of a circular economy and energy recycling in Europe. *Energy* **2017**, *141*, 2013–2044. [CrossRef]
29. Li, H.T.; Zhang, H.; Li, K.J.; Zhang, J.L.; Sun, M.M.; Su, B.X. Catalytic graphitization of coke carbon by iron: Understanding the evolution of carbon Structure, morphology and lattice fringes. *Fuel* **2020**, *279*, 118531. [CrossRef]